ADVANCED MATERIALS
www.advmat.de

Structure Engineering of a Lanthanide-Based Metal–Organic Framework for the Regulation of Dynamic Ranges and Sensitivities for Pheochromocytoma Diagnosis

Ji-Na Hao, Dechao Niu, Jinlou Gu, Shaoliang Lin, Yongsheng Li,* and Jianlin Shi*

Exploring innovative technologies to precisely quantify biomolecules is crucial but remains a great challenge for disease diagnosis. Unfortunately, the humoral concentrations of most biotargets generally vary within rather limited scopes between normal and pathological states, while most literature-reported biosensors can detect large spans of targets concentrations, but are less sensitive to small concentration changes, which consequently make them mostly unsatisfactory or even unreliable in distinguishing positives from negatives. Herein, a novel strategy of precisely quantifying the small concentration changes of a certain biotarget by editing the dynamic ranges and sensitivities of a lanthanide-based metal–organic framework (Eu-ZnMOF) biosensor is reported. By elaborately tailoring the biosensor's structure and surface areas, the tunable Eu-ZnMOF is developed with remarkably enhanced response slope within the "optimized useful detection window," enabling it to serve as a powerful signal amplifier (87.2-fold increase) for discriminating the small concentration variation of urinary vanillylmandelic acid (an early pathological signature of pheochromocytoma) within only three times between healthy and diseased subjects. This study provides a facile approach to edit the biosensors' performances through structure engineering, and exhibits promising perspectives for future clinical application in the non-invasive and accurate diagnosis of severe diseases.

Precise detection of disease-related biomolecules is of vital importance for the clinical diagnostics, especially for the early-stage cancer theranostics.[1–4] Generally, the clinically relevant concentration variations of most disease markers in biological samples are very small, which spans even less than an order of magnitude between healthy people and patients.[5–7] For example, vanillylmandelic acid (VMA), which serves as a clinical indicator for pheochromocytoma (PHEO, a neuroendocrine tumor arising from the chromaffin cells of the adrenal medulla), is produced as 1.0–2.9 × 10^{-5} mol L^{-1} by normal physiological process in healthy people, and only has a threefold increase during the pathological process of PHEO.[8,9] Such tiny concentration changes are very hard to be precisely distinguished and easy to bring in false-positive/negative diagnostic results. Therefore, exploring biosensors that have robust and ultrasensitive responses to small changes in target concentration is highly desirable for precise diagnosis. Great efforts have been devoted to develop biodetection methods with different signal transductions, high specificity, and low detection limits. However, a significant limitation of the most reported biosensors is that their robust signal-output transition often requires a large fixed span of targets concentration, which is usually not the "useful detection window" and far wider than the inherent physiological ranges of the biotargets.[10,11] Consequently, they are insensitive to a small concentration change of the targets within the physiologically narrow range, making them less effective or non-effective to precisely detect biotargets and unreliable to differentiate the positives from negatives for disease diagnosis. To overcome the above limitations and improve the diagnostic precision for biomolecules, we attempt to design an optical biosensor with tunable, optimal detection ranges and sensitivities, which can provide an ultrasensitive assay to a small concentration change of the disease-related biomolecules within a desired concentration window.

Luminescent metal–organic frameworks (MOFs), as a kind of the crystalline porous materials featuring with structural tunability and functional diversity, have been proven as the promising sensing candidates.[12–17] Their tailorable surface areas and porosities, which play an important role in the enrichment of analytes,[12,13] provide distinct advantages in editing and optimizing the detection performances of MOFs. However, the literature has seen little exploration regarding the engineering of the MOF structure properties to regulate the dynamic ranges and sensitivities of MOF-based probes, though they have been

Dr. J.-N. Hao, Dr. D. Niu, Prof. J. Gu, Prof. S. Lin, Prof. Y. Li, Prof. J. Shi
Laboratory of Low-Dimensional Materials Chemistry
Key Laboratory for Ultrafine Materials of Ministry of Education
Shanghai Engineering Research Center of Hierarchical Nanomaterials
School of Materials Science and Engineering
Frontier Science Center of the Materials Biology and Dynamic Chemistry
East China University of Science and Technology
Shanghai 200237, P. R. China
E-mail: slin@ecust.edu.cn; ysli@ecust.edu.cn
Prof. J. Shi
State Key Laboratory of High Performance Ceramics
and Superfine Microstructure
Shanghai Institute of Ceramics
Chinese Academy of Sciences
Shanghai 200050, P. R. China
The ORCID identification number(s) for the author(s) of this article can be found under https://doi.org/10.1002/adma.202000791.

DOI: 10.1002/adma.202000791

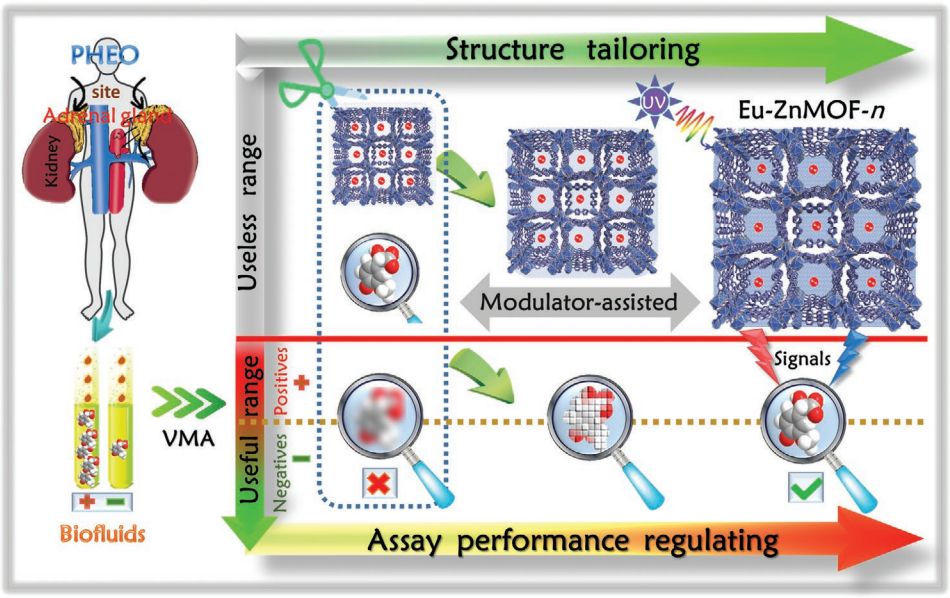

Scheme 1. Schematic illustration for structure tailoring of the Eu-ZnMOF-*n* to program and optimize its analysis performance for the PHEO's indicator (VMA).

widely investigated and developed for detecting various analytes.[18–30] Moreover, only a few of these MOF-based sensors are used for recognizing disease-related markers,[23,24,28] and they are also limited to an unoptimizable detection range with insufficient responses to small changes of the targets concentration, which is unsatisfactory for precise diagnosis of disease. Herein, we report a novel strategy to engineer a luminescent lanthanide-based metal–organic framework (Eu-ZnMOF) biosensor with tunable detection performances for tracing the overexpressed VMA in urine (**Scheme 1**). By rationally tailoring the structure and surface areas of the sensor, its quantitative linear range is well edited to the "useful VMA window" with remarkably steep response slope, making it highly precise for discriminating the small change of VMA concentration between the positives and negatives. In addition, this optimized sensor simultaneously provides multiple approaches for rapid quantification of VMA under complex biological urine environments. With the optimized dynamic range, sensitivity, and multimode assay, our fabricated platform can inherently improve the analysis reliability and largely avoid the false-positive and negative results.

The formation of editable Eu-ZnMOFs was started from the synthesis of ZnMOFs as initiator. The ZnMOFs were synthesized by solvothermal reaction with various feed ratios of nitric acid to zinc acetate and denoted as ZnMOF-*n*, where *n* (*n* = 1–4) represents the increasing modulator in the synthesis. In **Figure 1**a, it is found that the diffraction peaks of ZnMOFs match well with the simulated one,[31] indicating that the as-prepared materials are topologically identical and have high crystalline-phase purity. Besides, the intensity of Bragg diffraction peak at 4.6° gradually enhances along with the increase of acid modulator in the synthesis of ZnMOFs, implying a crystallization promotion effect of the modulator. The N_2 sorption isotherms (Figure 1b) show that the saturated N_2 uptakes for ZnMOF-*n* gradually increase with *n* values, and thus their Brunauer–Emmett–Teller (BET) surface areas and pore volumes increase from 526 to 1043 $m^2\ g^{-1}$ (Figure 1c) and from 0.26 to 0.43 $cm^3\ g^{-1}$ (Table S1, Supporting Information), respectively. These reveal that the incorporation of more modulator during the reaction can effectively increase the surface areas and pore volumes of the fabricated ZnMOF. This is because the acid modulator can slow down crystal growth to produce higher degrees of crystallinity[32] and thus generally leads to a more ordered molecular arrangement and pore-structure for porous materials with larger BET surface areas and pore volumes.[33] Besides, the large amount of acid can also facilitate the formation of defects in crystalline materials through affecting the coordination behaviors between metal ions and ligands.[34,35] The defects in the structure were further studied by thermogravimetric analyses. As shown in Figure S1, Supporting Information, the weight loss in the temperature range of 305–700 °C corresponding to the linker/framework combustion gradually decreases from ZnMOF-1 to ZnMOF-4, indicating that the ligands content in the materials were gradually reduced and more defects were thus created.[34,35] More defects in materials present larger BET surface areas and pore volumes accordingly. Therefore, the increase of the BET surface areas and pore volumes can be ascribed to the combination effect of higher crystallinity and more defects. Then, the ZnMOF-*n* samples were exchanged with photoactive europium nitrate via dimethylamine cations within the framework to yield luminescent Eu-ZnMOF-*n* materials, which are isostructural with the pristine ZnMOFs, as demonstrated in Figure 1a. Inductively coupled plasma optical emission spectra analysis of both the reaction supernatant and the resultant Eu-ZnMOF-*n* (*n* = 1–4) reveals the coexistence of Eu^{3+} and Zn^{2+} cations in the material (Table S2, Supporting Information) without Zn in the supernatant. Similar relative molar ratios of Eu^{3+}:Zn^{2+} in the four samples are also revealed, which are determined to be ≈1:13. ^1H nuclear magnetic resonance (NMR) spectra (Figure S2, Supporting Information) shows that the chemical shift of dimethylamine at 2.54 ppm in ZnMOF-4 disappeared after exchanging Eu. This evidence

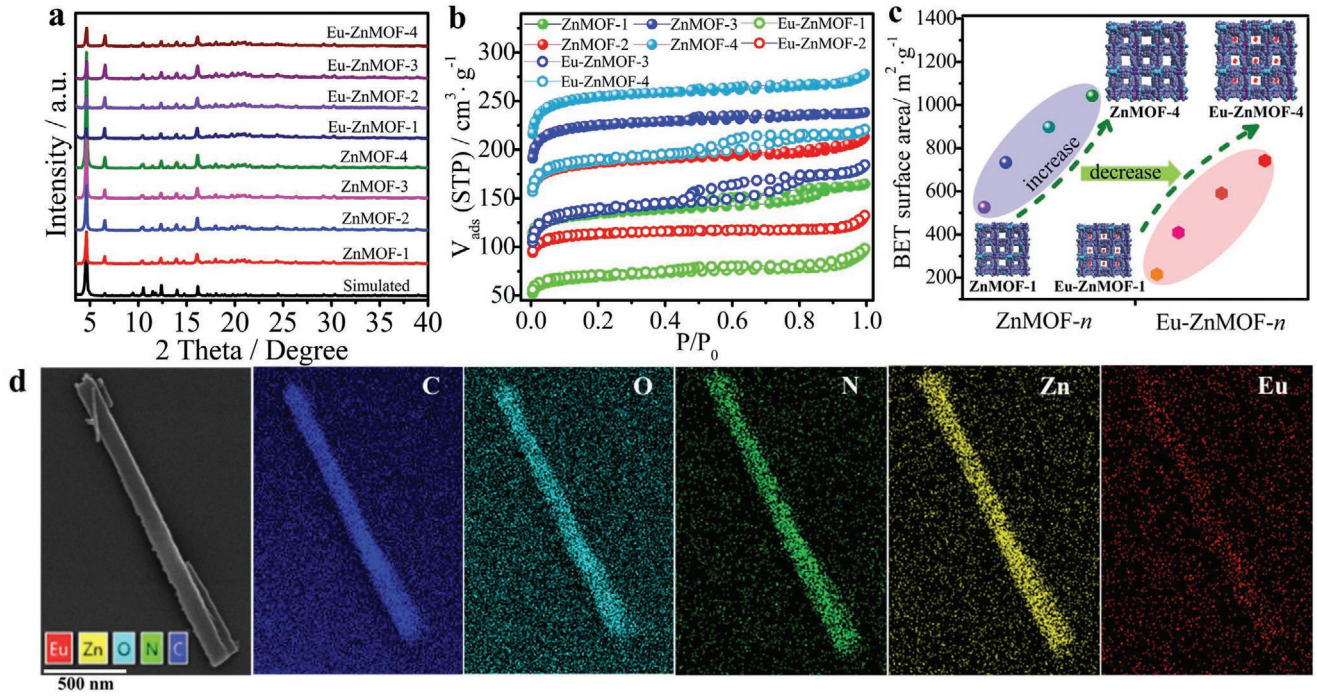

Figure 1. Characterizations of ZnMOF-*n* and Eu-ZnMOF-*n*. a) PXRD patterns of simulated pristine ZnMOF, and experimental ZnMOF-*n*, and Eu-ZnMOF-*n* (*n* = 1–4). b,c) Nitrogen adsorption/desorption isotherms at 77 K and the variation tendency of BET surface area for ZnMOF-*n* and Eu-ZnMOF-*n* (*n* = 1–4). d) SEM images and EDS mapping for different elements of Eu-ZnMOF-4.

demonstrate that all the dimethylamine ions (2 cations per Zn_8 unit)[31] in the ZnMOF have been successfully exchanged by 0.615 Eu^{3+} per unit. Energy-dispersive X-ray spectroscopy (EDS) mapping shows an even distribution of the post-exchanged Eu element in the Eu-ZnMOF material (Figure 1d). The successful exchange of Eu^{3+} in ZnMOF-*n* results in a reduced BET surface area of 215, 409, 591, and 742 $m^2\ g^{-1}$ (Figure 1b,c) as well as a decreased pore volume (Table S1, Supporting Information) for Eu-ZnMOF-*n* (*n* = 1–4, respectively), compared with that of the corresponding ZnMOF-*n*. This can be attributed to the decreased crystallinity of the Eu-ZnMOF-*n* samples, as shown in Figure 1a. The decreased crystallinity indicates less-ordered molecules-arrangement and pore-structure, and thus produced a lower BET surface and pore volume.[36] Figure S3, Supporting Information, reveals that a small amount of mesopores exist in the ZnMOF-*n* and Eu-ZnMOF-*n* (*n* = 3 and 4), which likely originates from the relatively large-scale or correlated defects in the materials, causing the non-typical type-I isotherms in these materials.[35] After the successful fabrication of Eu-ZnMOF-*n*, their luminescence properties were investigated (Figure S4, Supporting Information). Irradiated with a laboratory UV lamp (254 nm), the Eu-ZnMOF-*n* suspensions display the red colors of Eu^{3+} (Figure S4a, Supporting Information), which is visible to naked eyes as a qualitative indication of sensitization effect. The excitation spectra of Eu-ZnMOF-*n* recorded at the Eu^{3+} emission center (615 nm) show a broad band located at 330 nm, assignable to the $\pi \rightarrow \pi^*$ transition of the 4,4′-biphenyldicarboxylic acid (BPDC) linkers. Upon excitation at 330 nm, the emission spectra of Eu-ZnMOF-*n* (Figure S4b–e, Supporting Information) feature two kinds of signals: the characteristic sharp emissions of Eu^{3+} at 579, 592, 615, 652, and 697 nm corresponding to $^5D_0 \rightarrow {}^7F_J$ (J = 1–4) transitions and the ligand-based broad emission in the blue-colored range of 370–570 nm (Figure S5, Supporting Information), implying that the ligand (BPDC) partially transfers its absorbed energy to Eu^{3+}. Moreover, the fabricated system shows high pH toleration in both structure and luminescence within the humoral relevant pH range (4.6–8.0), as evidenced by the negligible changes in either crystalline integrity (Figure S6, Supporting Information) or the luminescence intensities (Figures S7 and S8, Supporting Information) of both the Eu-ZnMOF-1 and Eu-ZnMOF-4, enabling it to be competent for application in physiological environment. Benefitting from the excellent optical performances and susceptible energy transfer between the two emitters, the Eu-ZnMOFs with good chemical stability and tailorable structure properties can be potentially used as bioprobes for the target in body fluids.

As a proof-of-concept experiment, the analysis capability of the Eu-ZnMOF-*n* (*n* = 1–4) for VMA was investigated. As shown in Figures S9–S12, Supporting Information, upon an increase of VMA concentration (*C*), the emission signal I at ≈433 nm (I_1) becomes conspicuous, while the intensity of emission signal II at 615 nm (I_2) gradually decreases in the Eu-ZnMOF-*n* (*n* = 1–4) under a single excitation of 330 nm. The multi-signal intensities (I_1/I_0, I_2/I_0, and I_1/I_2, I_0: the original intensity of the corresponding signal) of the Eu-ZnMOF-*n* were plotted as a function of VMA concentration (*C*), which corresponds to three readout passways of "signal-on" (**Figure 2**a), "signal-off" (Figure 2b), and "signal-on/off" (Figure 2c), respectively. It is observed that a steeper and narrower dose-response curve for each of the three passways is obtained for the Eu-ZnMOF-*n* (*n* = 1–4), suggesting that the probe with higher surface area presents stronger and more sensitive multi-responses to lower VMA content. The

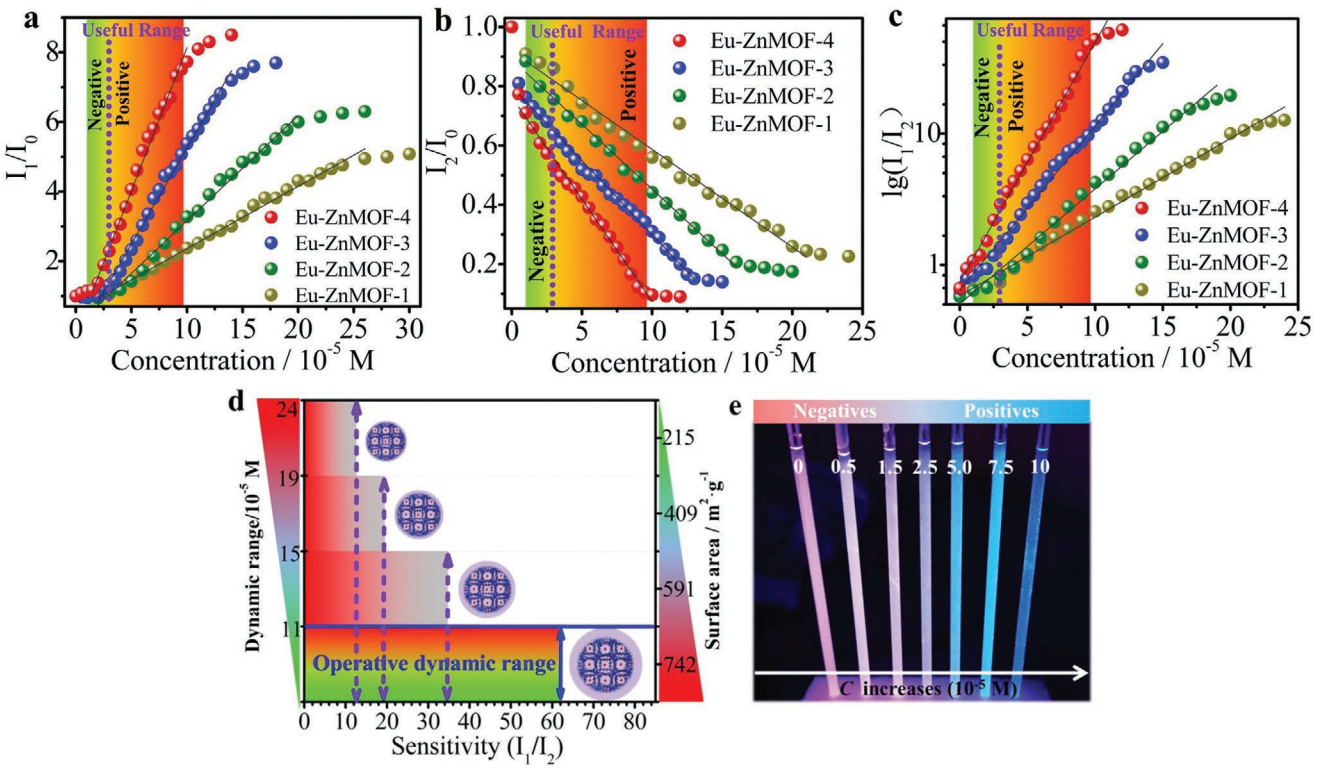

Figure 2. Editable performances of the probe for the determination of VMA concentration. a–c) The dose-response curves of the dual signaling Eu-ZnMOF-*n* (*n* = 1–4) under signal-on (I_1/I_0, (a)), signal-off (I_2/I_0, (b)), and signal-on/off (I_1/I_2, (c)) modes at increased concentrations of VMA (*C*). I_0 in (a) and (b) refers to the original intensity of signal I and signal II, respectively; lg in (c) represents the common logarithm "$\log_{10}$". d) The structure–property relationship of the probe's surface area to its dynamic range and sensitivity. e) Color-coded digital array of Eu-ZnMOF-*n* probe after being treated with increased VMA concentrations under irradiation with a UV lamp (λ_{ex} = 254 nm).

I_1/I_0–*C* growth curve, I_2/I_0–*C* decrease curve, and $\lg(I_1/I_2)$–*C* plot of the Eu-ZnMOF-*n* all show a good response linearity at a specific concentration window. The linear detection ranges, fitted regression equations, and calculated limit of detections of the Eu-ZnMOF-*n* probes for VMA were compared in Table S3, Supporting Information and Figure 2d. It is found that by increasing the structural surface area of the probe from Eu-ZnMOF-1 to Eu-ZnMOF-4, its linear dynamic range is obviously narrowed by more than a half and simultaneously its input–output curve slope is enhanced by 4.6, 2.0 and 3.0 times for I_1/I_0, I_2/I_0, and $\lg(I_1/I_2)$ versus *C*, respectively. This can be explained by the fact that the sensor with higher surface area/pore volume can preconcentrate more target molecules within the framework and thus exhibits higher response efficiency.[12,13,37,38] Moreover, the molecular size of VMA (9.359 × 8.263 × 7.079 Å, Figure S13, Supporting Information) was calculated to be smaller than the channel window of Eu-ZnMOF-*n* (10 × 10 Å), which offers convenience for enriching VMA into pores. To verify such a preconcentration effect, the Eu-ZnMOF-*n* was soaked in a known concentration (C_0) of VMA to determine the amount of analyte it absorbed. Based on the adsorption data (Figure S14, Supporting Information), the concentration of VMA in the supernatant (C_s) was measured after the removal of Eu-ZnMOF-*n*, and its content within Eu-ZnMOF-*n* (C_{MOF}) was calculated by the equation in the Experimental Section (see Supporting Information). Thus, the preconcentration factor of the Eu-ZnMOF-*n* for VMA, defined as C_{MOF}/C_s, were calculated to be 533, 919, 1938, and 3800, respectively, well demonstrating the higher enrichment effect of the sensor with higher surface area/pore volume. With this structure tailoring strategy, the quantitative linear range of the Eu-ZnMOF-4 was optimized to the biologically relevant concentration window (10^{-5}–10^{-4} M), which well matched with the narrow VMA range for healthy (1.0–2.9 × 10^{-5} M) and diseased (3.0–9.5 × 10^{-5} M) subjects.[9] Meanwhile, the sensitivities of the probe were highly enhanced for the three detection modes of "signal-on", "signal-off", and "signal-on/off" over such a narrow concentration range. Such optimized performances of Eu-ZnMOF-4 enable it to be a powerful signal amplifier for sensing VMA concentration even with a tiny change, and thus greatly improve its precision of differentiating positives from negatives. Moreover, the integrating of three quantitative detection paths (Equations (S1)–(S3) in Table S3, Supporting Information) for VMA in a single sensing interface provides multiple insurances on the assay and thus guarantees the quantitative reliability of the Eu-ZnMOF-4 probe. The kinetic analysis (Figure S15, Supporting Information) of the optimized Eu-ZnMOF-4 sensor indicates that both the "signal-on" and "signal-off" responses induced by VMA stimulus (2.5, 5.0, 7.5 and 10 × 10^{-5} M) only take a few seconds (15 s) to reach equilibrium, allowing its real-time monitoring of VMA concentration variation. Such instantaneous and opposite variations of the blue-colored signal I and red-colored signal II from Eu-ZnMOF-4

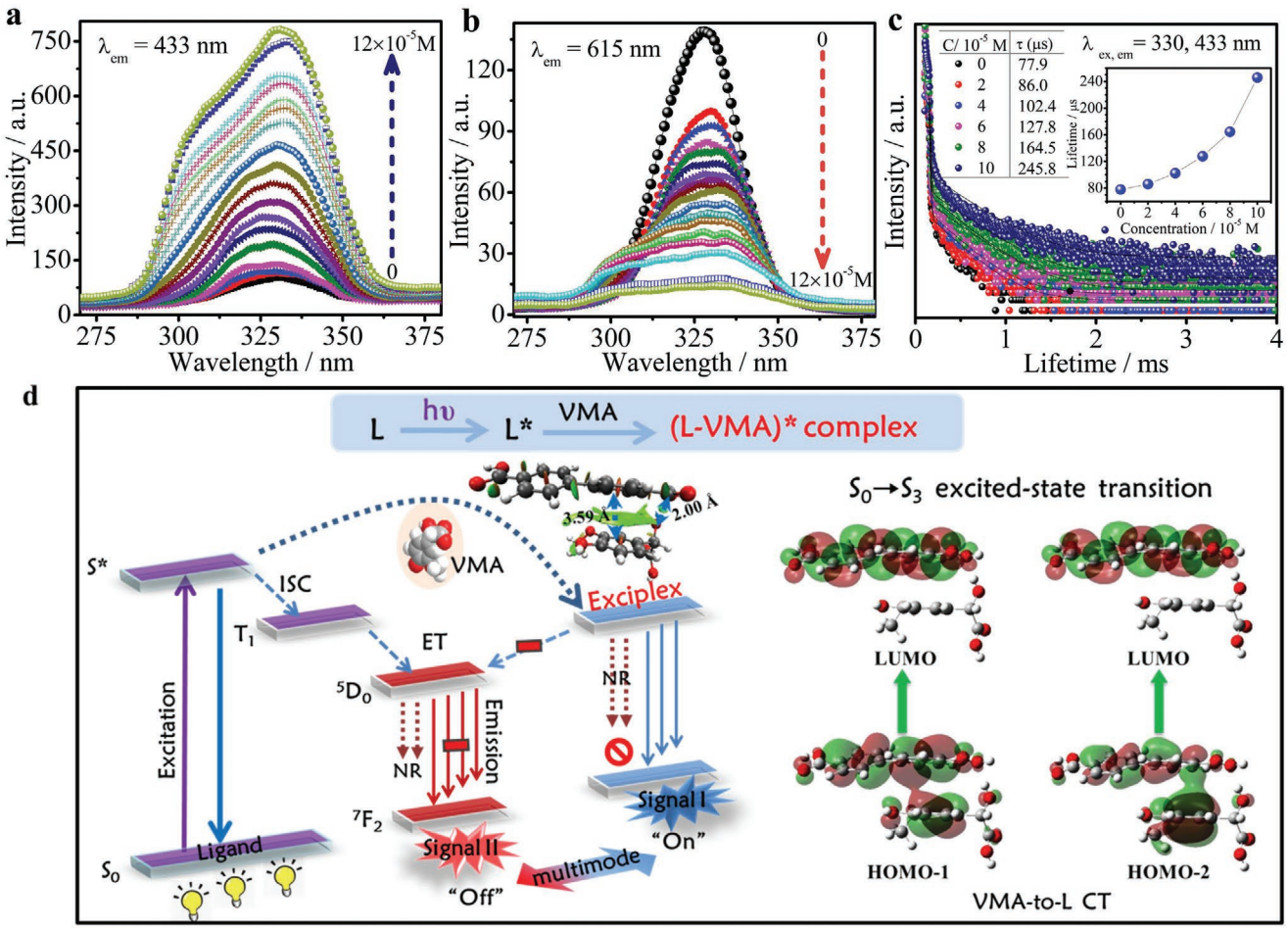

Figure 3. Luminescence switching mechanism of the probe for VMA. a,b) The gradually widened excitation spectra of Eu-ZnMOF-*n* monitored at both 433 and 615 nm upon incremental addition of VMA. c) Lifetimes of Eu-ZnMOF-*n* at 433 nm in response to the concentration variations of VMA in aqueous solutions (λ_{ex} = 330 nm). d) Diagram of the "exciplex" mechanism governing the switch-on (signal I) and switch-off (signal II) responses of the Eu-ZnMOF-*n* toward VMA, and the noncovalent interactions (binding energy: 11.52 kcal mol^{-1}) between the BPDC ligand and VMA (left: ISC, intersystem crossing; ET, energy transfer; and NR, non-radiative transition). The right diagram of (d) shows the excited-state transitions of [L-VMA] complex originating from the HOMO-1/2 to the LUMO (CT, charge transfer, HOMO, highest occupied molecular orbital, LUMO, lowest unoccupied molecular orbital).

result in obviously visible luminescence color transitions from light-red to cyan as the VMA concentration increases, yielding a color-coded digital array (Figure 2e). In this array, each color rod corresponds to a specific VMA concentration, providing an eye readable approach to roughly distinguish negatives from positives. The mechanism governing this stimuli-responsive behavior was further explored. As demonstrated in Figure S16 and Table S4, Supporting Information, neither the structure transformation of the Eu-ZnMOF-4 nor the content variation of signal-reporter (Eu^{3+}) in it contributes to its stimuli-response capability for VMA. Notably, the ligand-based emission in both Eu-ZnMOF-4 (signal I, Figure S17, Supporting Information) and pure ZnMOF-4 (Figure S18, Supporting Information) exhibits an obvious bathochromic shift of ≈15 nm upon addition of VMA. At the same time, the excitation bands of Eu-ZnMOF-4 monitored at either 433 or 615 nm (**Figure 3**a,b; Figure S19, Supporting Information) are apparently broadened with their full width at half-maximum gradually increasing by ≈20 nm (Table S5, Supporting Information) with VMA content increasing from 0 to 12 × 10^{-5} M, as calculated by Gaussian fitting. These suggest that an exciplex with a lower-lying excited-state energy level than that of the ligand is formed between the MOF's ligand (L, BPDC) and VMA during the excitation.[12,39,40] Figure 3c reveals that the luminescence decay of the Eu-ZnMOF-4 probe at 433 nm gradually increases from 77.9 to 245.8 μs. A similar lifetime increment is also observed for pure ZnMOF-4 at 433 nm with the addition of VMA (Figure S20, Supporting Information). While, the luminescence decays of the Eu-ZnMOF-4 at 615 nm almost do not change upon VMA stimulus (Figure S21, Supporting Information), indicating the static quenching interaction of Eu^{3+} with VMA in the ground state.[18] These further confirm that VMA is interacted with the ligand (Figure 3d) in the excited state to form the [L-VMA]* exciplex, which can largely reduce the nonradiative decay in the photoluminescence process and thus remarkably increase the emission of signal I in Eu-ZnMOF-4.[41] Generally, the exciplex was formed by the intermolecular charge/electron-transfer reaction during the excitation. To verify this, the excited-state charge transfer (ESCT) of the [L-VMA] complex was investigated by theoretical calculation. As shown in Table S6, Supporting

Information, the $S_0 \rightarrow S_3$ is the main excited transition process in [L-VMA] complex since it has the largest oscillator strength among all the possible excited transitions and its corresponding calculated absorption wavelength of 304 nm is very close to the experimental excitation value (330 nm). The $S_0 \rightarrow S_3$ mainly has two different electron transition paths, in which HOMO-2→LUMO contributes 77.3% and HOMO-1→LUMO contributes 20.1%. As illustrated in Figure S22, Supporting Information, both HOMO-2 and HOMO-1 of [L-VMA] complex have obvious electron densities distribution on both VMA and ligand fragments. While, the electron densities of LUMO mainly distributed on the ligand (89.23%, Figure S23, Supporting Information). This indicates that both the HOMO-2→LUMO and HOMO-1→LUMO transitions involve abundant electron transfer from VMA to ligand during the $S_0 \rightarrow S_3$ excitation, providing the theoretic evidence that the presence of intermolecular charge/electron-transfer between the ligand and VMA during the excitation process. Thus, it can be concluded that the driving force to trigger the stimuli-behaviors of the probe for VMA is the formation of a strong fluorescent intermediate exciplex (i.e., ESCT complex) between the ligand and VMA, whose excited-state level is higher than that of $^5D_0$ of Eu^{3+}, but lower than that of the primitive ligand (Figure 3d). The lowered excited energy levels of the exciplex and its energy gap with Eu probably decrease the ligand-to-Eu energy transfer process. As a result, the ligand-centered emission (signal I) in Eu-ZnMOF-4 was substantially switched on and the Eu luminescence (signal II) was decreased by VMA (Figure 3d).

The Eu-ZnMOF-4 incubated with mimetic urine species was further used for control experiments to investigate its specific recognition for VMA. As shown in **Figure 4**a,b and Figure S24a, Supporting Information, the emission intensity variations (ΔI_1, ΔI_2, and $\Delta I_1/I_2$) obtained from blank and other potential interferences are similar and much less than that of VMA, demonstrating the high recognition specificity of Eu-ZnMOF for VMA over other coexisting species. Consistent with these spectra changes, VMA affords the most apparent color transition from red to cyan by naked-eye observations under a UV-lamp, whereas the others' outputs remain unchanged (Figure S24c, Supporting Information), endowing the sensor with visual identification capability for VMA. Motivated by these findings, the selectivity of Eu-ZnMOF-4 for VMA in the presence of these interferents was also checked. The proposed biosensor exhibits excellent performance for discriminating the VMA biotarget among the mixed analytes and artificial urine, as verified in Figure 4c,d and Figure S24b,d Supporting Information, which shows that the VMA-triggered significant changes in both I_1, I_2, I_1/I_2 intensities and output colors are hardly affected by the background of the various coexisting species and the artificial urine. These findings demonstrate that the Eu-ZnMOF-4 can act as a highly selective probe for VMA in mimicking urine environments without structure/composition changes (Figure S25, Supporting Information). The specificity of the Eu-ZnMOF-4 for VMA can be ascribed to the fact that the optimal geometry between the ligand and VMA is nearly the face-to-face orientation through π–π interaction with interface distance of 3.59 Å. This structure is very beneficial to the formation of the exciplex between the ligand and VMA. Such face-to-face arrangements, however, cannot be formed between the other interferents and the ligand to form the exciplex (Figure S26, Supporting Information). Therefore, the Eu-ZnMOF can specifically detect VMA among the various interferents.

To investigate the feasibility of this approach using in biological matrices, standardized urine samples spiked with VMA

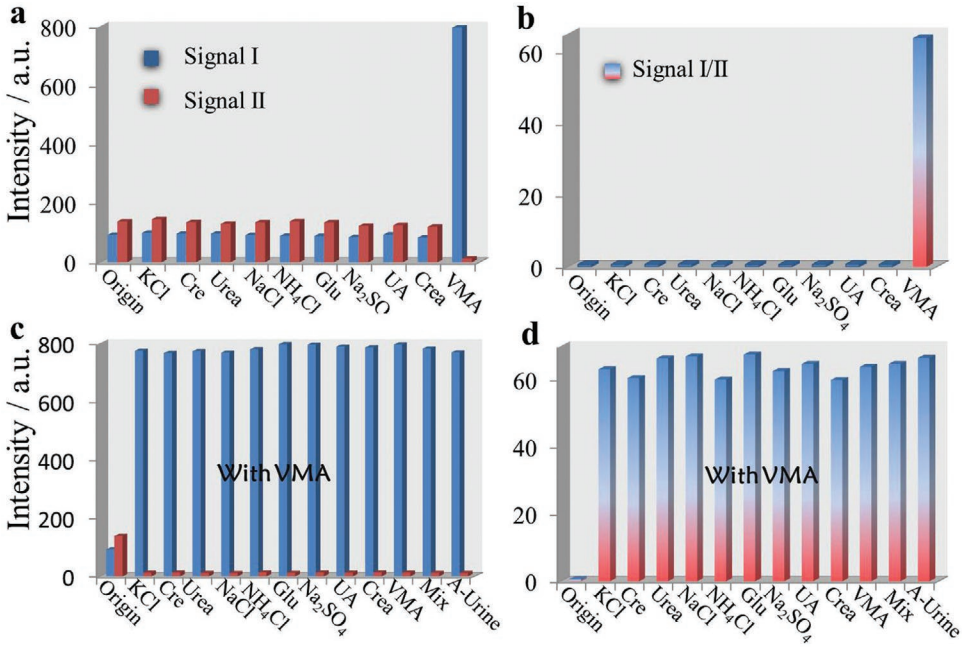

Figure 4. Specificity of Eu-ZnMOF-*n* for VMA. a,b) Emission intensity changes of signal I, II, and I/II from Eu-ZnMOF-*n* induced by VMA and various biologically coexisting species under the excitation of 330 nm. c,d) Luminescence intensity responses of signal I, II, and I/II from Eu-ZnMOF-*n* toward VMA in the presence of background of other various urine components (λ_{ex} = 330 nm).

Table 1. Analysis results of VMA in urine specimens by the optimized and multimode Eu-ZnMOF-*n* probe.

Urine samples	Spiked [10^{-5} M]	Measured by Equations (S1)–(S3)[a)] [10^{-5} M]	Recovery [%]	CV [%]	Output
A-1	1.5	1.54 ± 0.04	102.7	2.60	Faint
–	–	1.45 ± 0.05	96.7	3.45	–
–	–	1.37 ± 0.02	91.3	1.46	–
A-2	8.5	8.26 ± 0.13	97.2	1.57	Blue
–	–	8.63 ± 0.11	101.4	1.28	–
–	–	8.52 ± 0.09	100.2	1.05	–

[a)]All concentrations are expressed as the mean of six measurements ± standard deviation. Equations S1–S3 are found in Table S3 of the Supporting Information.

at different concentrations were analyzed by the optimized sensor that integrated three quantitative paths into a single detection interface. As summarized in **Table 1**, the VMA levels determined from the "turn-on", "turn-off", and "on/off" detection pathways are very close, providing multiple insurances on the assay and largely avoid the false results. The analytical recoveries (defined as the measured amount divided by the real spiked amount of VMA in urine specimen) of all the assays ranged from 91.3% to 102.7%, and the coefficient of variations (CVs) are in the range of 1.05% to 3.45%, both of which well satisfy the criteria (recoveries in the range of 90–110%, CVs less than 15%) set for the bioanalytical method validation.[42] This confirms the high assay accuracy and reliability of the proposed multimode bioprobe with tailored optimal dynamic range in urine. Our sensing strategy that has ultrasensitive multiple readouts over a narrow "optimal detection window" ensures the robust responses to a very small change in VMA concentration, allowing for the precise discrimination of positive and negative results and thus undoubtedly boosting the reliability of bioassays.

In summary, we have demonstrated a facile strategy to engineer a luminescent Eu-ZnMOF biosensor with editable quantitative dynamic ranges and sensitivities for precise identification of urinary VMA, which is the crucial indicator for the pheochromocytoma's clinical diagnosis. By elaborately tailoring the biosensor's structure and surface areas via the modulator, its dynamic range was optimized and narrowed to the "useful detection window" ($1.0–10 \times 10^{-5}$ M) of VMA, and its response slope/sensitivity within this narrow physiological range was highly enhanced. Such excellent features enabled the tailorable probe to possess an ultra-high quantitative luminescence response toward a very small concentration variation (signal increase of 87.2 folds over the range interval of 11×10^{-5} M) of VMA in urine, remarkably improving the diagnostic precision for pheochromocytoma disease. Moreover, this system also integrated three quantitative pathways into a single assay interface for rapid (15 s), and accurate (CVs < 3.45%) identification of VMA under complex urine environments, providing multiple insurances on the positive-/negative-diagnosis results and largely lowering the error rate. This work provides a facile strategy and significant inspirations for engineering the MOFs structure to tune and optimize their analysis performance for biotargets in human health monitoring.

Supporting Information

Supporting Information is available from the Wiley Online Library or from the author.

Acknowledgements

This work was financially supported by the National Key Research and Development Program of China (Grant No. 2018YFC1105702), the National Natural Science Foundation of China (Nos. 51621002, 21805087, 51873061, and 51972112), Shanghai Sailing Program (18YF1405900), China Postdoctoral Science Foundation (2017M621383), Program of Shanghai Academic/Technology Research Leader (18XD1401400), Basic Research Program of Shanghai (17JC1404702, 19JC1411700), Leading Talents in Shanghai in 2018, and the 111 project (B14018).

Conflict of Interest

The authors declare no conflict of interest.

Keywords

metal–organic frameworks, pheochromocytoma diagnosis, tailorable structures, tunable biosensors, vanillylmandelic acid

Received: February 4, 2020
Revised: March 15, 2020
Published online:

[1] A. Nakamura, N. Kaneko, V. L. Villemagne, T. Kato, J. Doecke, V. Doré, C. Fowler, Q.-X. Li, R. Martins, C. Rowe, T. Tomita, K. Matsuzaki, K. Ishii, K. Ishii, Y. Arahata, S. Iwamoto, K. Ito, K. Tanaka, C. L. Masters, K. Yanagisawa, *Nature* **2018**, *554*, 249.
[2] J. D. Cohen, L. Li, Y. Wang, C. Thoburn, B. Afsari, L. Danilova, C. Douville, A. A. Javed, F. Wong, A. Mattox, R. H. Hruban, C. L. Wolfgang, M. G. Goggins, M. D. Molin, T.-L. Wang, J. J. Mansfield, S. M. Hanash, M. Falconi, P. J. Allen, S. Zhou, C. Bettegowda, L. Diaz, C. Tomasetti, K. W. Kinzler, B. Vogelstein, A. M. Lennon, N. Papadopoulos, *Science* **2018**, *359*, 926.
[3] M. J. Baker, S. R. Hussain, L. Lovergne, V. Untereiner, C. Hughes, R. A. Lukaszewski, G. Thiefin, G. D. Sockalingum, *Chem. Soc. Rev.* **2016**, *45*, 1803.
[4] X. Zhou, P. Cao, Y. Zhu, W. Lu, N. Gu, C. Mao, *Nat. Mater.* **2015**, *14*, 1058.
[5] S. Liu, Y. Chen, P. Wan, C. Zhou, S. Zhang, H. Mo, *Electrochim. Acta* **2016**, *216*, 528.
[6] G. B. Mills, W. H. Moolenaar, *Nat. Rev. Cancer* **2003**, *3*, 582.
[7] G. Ammanath, U. H. Yildiz, A. Palaniappan, B. Liedberg, *ACS Appl. Mater. Interfaces* **2018**, *10*, 7730.
[8] Y. Shen, J. Lu, Q. Tang, Q. Guan, Z. Sun, H. Li, L. Cheng, *J. Chromatogr. B* **2015**, *1002*, 92.
[9] A. Nemeckova-Makrlikova, F.-M. Matysik, T. Navratil, J. Barek, V. Vyskocil, *Electroanalysis* **2019**, *31*, 303.
[10] F. Ricci, A. Vallee-Belisle, A. J. Simon, A. Porchetta, K. W. Plaxco, *Acc. Chem. Res.* **2016**, *49*, 1884.
[11] D. Gareau, A. Desrosiers, A. Vallee-Belisle, *Nano Lett.* **2016**, *16*, 3976.
[12] L. E. Kreno, K. Leong, O. K. Farha, M. Allendorf, R. P. Van Duyne, J. T. Hupp, *Chem. Rev.* **2012**, *112*, 1105.
[13] W. P. Lustig, S. Mukherjee, N. D. Rudd, A. V. Desai, J. Li, S. K. Ghosh, *Chem. Soc. Rev.* **2017**, *46*, 3242.

[14] Y. Cui, J. Zhang, H. He, G. Qian, *Chem. Soc. Rev.* **2018**, *47*, 5740.
[15] S. Wu, H. Min, W. Shi, P. Cheng, *Adv. Mater.* **2020**, *32*, 1805871.
[16] R. Haldar, L. Heinke, C. Wöll, *Adv. Mater.* **2019**, *2019*, 1905227.
[17] J.-N. Hao, X. Xu, H. Fei, L. Li, B. Yan, *Adv. Mater.* **2018**, *30*, 1705634.
[18] B. Wang, P. Wang, L.-H. Xie, R.-B. Lin, J. Lv, J.-R. Li, B. Chen, *Nat. Commun.* **2019**, *10*, 3861.
[19] A. Mallick, A. M. El-Zohry, O. Shekhah, J. Yin, J. T. Jia, H. Aggarwal, A.-H. Emwas, O. F. Mohammed, M. Eddaoudi, *J. Am. Chem. Soc.* **2019**, *141*, 7245.
[20] Y. Luo, C. Li, W. Zhu, X. Zheng, Y. Huang, Z. Lu, *Angew. Chem., Int. Ed.* **2019**, *58*, 6280.
[21] J. Xie, Y. Wang, W. Liu, X. Yin, L. Chen, Y. Zou, J. Diwu, Z. Chai, T. E. Albrecht-Schmitt, G. Liu, S. Wang, *Angew. Chem., Int. Ed.* **2017**, *56*, 7500.
[22] L. Chen, J.-W. Ye, H.-P. Wang, M. Pan, S.-Y. Yin, Z.-W. Wei, L.-Y. Zhang, K. Wu, Y.-N. Fan, C.-Y. Su, *Nat. Commun.* **2017**, *8*, 15985.
[23] Y. Wang, Q. Liu, Q. Zhang, B. Peng, H. Deng, *Angew. Chem., Int. Ed.* **2018**, *57*, 7120.
[24] J.-N. Hao, Y. Li, *Adv. Funct. Mater.* **2019**, *29*, 1903058.
[25] B. Gui, Y. Meng, Y. Xie, J. Tian, G. Yu, W. Zeng, G. Zhang, S. Gong, C. Yang, D. Zhang, C. Wang, *Adv. Mater.* **2018**, *30*, 1802329.
[26] J.-N. Hao, B. Yan, *Adv. Funct. Mater.* **2017**, *27*, 1603856.
[27] S. Y. Zhang, W. Shi, P. Cheng, M. J. Zaworotko, *J. Am. Chem. Soc.* **2015**, *137*, 12203.
[28] S. Wu, Y. Lin, J. Liu, W. Shi, G. Yang, P. Cheng, *Adv. Funct. Mater.* **2018**, *28*, 1707169.
[29] Z. Han, K. Wang, Y. Guo, W. Chen, J. Zhang, X. Zhang, G. Siligardi, S. Yang, Z. Zhou, P. Sun, W. Shi, P. Cheng, *Nat. Commun.* **2019**, *10*, 5117.
[30] K. Zhang, X. Xie, H. Li, J. Gao, L. Nie, Y. Pan, J. Xie, D. Tian, W. Liu, Q. Fan, H. Su, L. Huang, W. Huang, *Adv. Mater.* **2017**, *29*, 1701804.
[31] J. An, S. J. Geib, N. L. Rosi, *J. Am. Chem. Soc.* **2009**, *131*, 8376.
[32] S. Yuan, L. Feng, K. Wang, J. Pang, M. Bosch, C. Lollar, Y. Sun, J. Qin, X. Yang, P. Zhang, Q. Wang, L. Zou, Y. Zhang, L. Zhang, Y. Fang, J. Li, H.-C. Zhou, *Adv. Mater.* **2018**, *30*, 1704303.
[33] P. Yang, Q. Zhuang, Y. Li, J. Gu, *Chem. Commun.* **2019**, *55*, 14902.
[34] S. Dissegna, K. Epp, W. R. Heinz, G. Kieslich, R. A. Fischer, *Adv. Mater.* **2018**, *30*, 1704501.
[35] Z. Fang, B. Bueken, D. E. De Vos, R. A. Fischer, *Angew. Chem., Int. Ed.* **2015**, *54*, 7234.
[36] Z. Wang, Y. Huang, J. Yang, Y. Li, Q. Zhuang, J. Gu, *Dalton Trans.* **2017**, *46*, 7412.
[37] M. M. Wanderley, C. Wang, C.-D. Wu, W. Lin, *J. Am. Chem. Soc.* **2012**, *134*, 9050.
[38] B. Wang, X.-L. Lv, D. Feng, L.-H. Xie, J. Zhang, M. Li, Y. Xie, J.-R. Li, H.-C. Zhou, *J. Am. Chem. Soc.* **2016**, *138*, 6204.
[39] M. D. Allendorf, C. A. Bauer, R. K. Bhakta, R. J. T. Houk, *Chem. Soc. Rev.* **2009**, *38*, 1330.
[40] N. C. Yang, D. M. Shold, B. Kim, *J. Am. Chem. Soc.* **1976**, *98*, 6587.
[41] J.-C. G. Bünzli, *Chem. Rev.* **2010**, *110*, 2729.
[42] S. Zhou, W. Zheng, Z. Chen, D. Tu, Y. Liu, E. Ma, R. Li, H. Zhu, M. Huang, X. Chen, *Angew. Chem., Int. Ed.* **2014**, *53*, 12498.